

Achieving Remarkable Activity and Durability toward Oxygen Reduction Reaction Based on Ultrathin Rh-Doped Pt Nanowires

Hongwen Huang,[†] Kan Li,[†] Zhao Chen,[†] Laihao Luo,[†] Yuqian Gu,[†] Dongyan Zhang,[†] Chao Ma,[†] Rui Si,^{*,‡} Jinlong Yang,[†] Zhenmeng Peng,^{*,§} and Jie Zeng^{*,†}

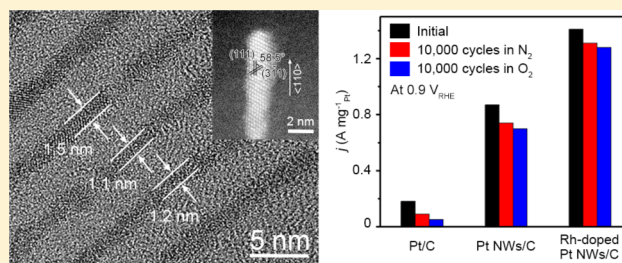
[†]Hefei National Laboratory for Physical Sciences at the Microscale, Key Laboratory of Strongly-Coupled Quantum Matter Physics of Chinese Academy of Sciences, Department of Chemical Physics, University of Science and Technology of China, Hefei, Anhui 230026, PR China

[‡]Shanghai Synchrotron Radiation Facility, Shanghai Institute of Applied Physics, Chinese Academy of Sciences, Shanghai 201204, PR China

[§]Department of Chemical and Biomolecular Engineering, University of Akron, Akron, Ohio 44325, United States

S Supporting Information

ABSTRACT: The research of active and sustainable electrocatalysts toward oxygen reduction reaction (ORR) is of great importance for industrial application of fuel cells. Here, we report a remarkable ORR catalyst with both excellent mass activity and durability based on sub 2 nm thick Rh-doped Pt nanowires, which combine the merits of high utilization efficiency of Pt atoms, anisotropic one-dimensional nanostructure, and doping of Rh atoms. Compared with commercial Pt/C catalyst, the Rh-doped Pt nanowires/C catalyst shows a 7.8 and 5.4-fold enhancement in mass activity and specific activity, respectively. The combination of extended X-ray absorption fine structure analysis and density functional theory calculations reveals that the compressive strain and ligand effect in Rh-doped Pt nanowires optimize the adsorption energy of hydroxyl and in turn enhance the specific activity. Moreover, even after 10000 cycles of accelerated durability test in O₂ condition, the Rh-doped Pt nanowires/C catalyst exhibits a drop of 9.2% in mass activity, against a big decrease of 72.3% for commercial Pt/C. The improved durability can be rationalized by the increased vacancy formation energy of Pt atoms for Rh-doped Pt nanowires.



■ INTRODUCTION

Proton exchange membrane fuel cells (PEMFCs) have been recognized as a promising clean energy conversion technology for efficient power delivery in transportation and mobile devices.^{1–3} However, the commercialization of such technology has so far been hampered by the prohibitive cost of associated devices, because a large amount of precious platinum (Pt) is required as catalyst to mitigate the sluggish kinetics of the oxygen reduction reaction (ORR) at the cathode.^{4–10} One solution to lower the cost is to reduce the usage of Pt catalyst in PEMFCs by improving the mass activity toward ORR. To this end, a variety of strategies have emerged to enhance the utilization efficiency (UE) of Pt, e.g., reducing the particle size,^{11–15} synthesizing a core–shell structure with a cheaper metal as the core,^{16–18} and preparing hollow nanostructures.^{19–22} Besides, another method to improve the mass activity is to boost the specific activity of a catalyst by incorporating a transition metal into Pt-based catalysts,^{23–26} shaping the exposed facets,^{23,27} tuning the surface strain,^{28–31} and so on. The principle of these methods, intrinsically, was to optimize the binding energy of oxygenated species.³² Although a number of Pt-based catalysts with excellent mass activities have been successfully reported, most of these catalysts suffered

from the relatively mediocre durability. For example, the electrochemical active surface area (ECSA) of Pt octahedral nanocages reduced by 23% after 10 000 cycles.²⁰ The insufficient durability of these Pt-based catalysts is ascribed to the thermodynamically unstable structures that are generally needed for high mass activities, so it seems that there is a conflict between high mass activity and superior durability.³³

Indeed, another solution to reduce the cost of PEMFCs is to improve the long-term durability of Pt-based electrocatalysts at the cathode. Tuning the dimension of Pt-based catalysts represents an effective strategy to modify the durability by varying the symmetry and surface area contiguous to carbon support. For instance, Pt-based catalysts with one-dimensional (1D) structures, such as Pt nanowires (NWs), exhibited better durability toward ORR than that of their zero-dimensional counterparts.^{34–36} The higher stability is due to the asymmetry of the structure which suppresses physical ripening process, and a higher surface area in contact with the carbon support which strengthens the interaction between NWs and carbon support. In addition, the incorporation of specific metals into Pt-based

Received: January 30, 2017

Published: May 25, 2017

catalysts has recently been proved favorable to improve the durability.^{37,38} For example, decorating Pt catalysts with Au clusters contributed to resisting the dissolution of Pt atoms under potential cycling regimes, which thus greatly enhanced their ORR durability.³⁷ Besides, adding a small amount of Rh into Pt–Ni nanoparticles was reported to help stabilize the octahedral morphology and enhance the catalytic durability.³⁸ Inspired by the above analysis, we anticipated achieving a superior catalyst by combining the features of high UE of Pt atoms, anisotropic 1D nanostructure, and doping of Rh atoms.

Herein, we report a remarkable ORR catalyst with both excellent mass activity and durability based on sub 2 nm thick Rh-doped Pt NWs, which combine the merits of high UE of Pt atoms, anisotropic one-dimensional nanostructure, and doping of Rh atoms. Because of the ultrathin diameter of 1.3 nm, the UE of Pt atoms for the NWs was estimated to be as high as 48.6% using an approximate atomic model. The Rh-doped Pt NWs/C catalyst exhibits the great improvement in both mass activity and durability toward ORR with respect to those of Pt NWs/C catalyst and commercial Pt/C catalyst. The origin of enhancement in activity and durability was also elucidated by extended X-ray absorption fine structure (EXAFS) analysis and density functional theory (DFT) calculations.

EXPERIMENTAL SECTION

Synthesis of Rh-Doped Pt NWs. In a typical synthesis of Rh-doped Pt NWs, Rh(acac)₃ (3.2 mg, 0.008 mmol), Pt(acac)₂ (28.8 mg, 0.073 mmol), and DDAB (90.0 mg, 0.194 mmol) were dissolved in 4.0 mL of oleylamine. The formed solution was immersed in an oil bath and preheated to 180 °C for 5 min, followed by the addition of W(CO)₆ (10.0 mg). Afterward, the temperature was kept at 180 °C for 2 h. After the solution was cooled down to room temperature, the product was precipitated by ethanol, washed three times with hexane, and then redispersed in hexane.

Synthesis of Pt NWs. The Pt NWs were obtained by using the standard procedure except for the absence of Rh precursors.

Synthesis of Rh-Doped Pt NWs with Different Pt/Rh Atomic Ratios. The Rh-doped Pt NWs with different Pt/Rh atomic ratios were obtained by using the standard procedure except for the addition of different amounts of Pt(acac)₂ and Rh(acac)₃ as precursors. Specifically, Rh(acac)₃ (1.6 mg, 0.004 mmol) and Pt(acac)₂ (30.4 mg, 0.077 mmol) were used for the synthesis of Rh-doped Pt NWs with a Pt/Rh atomic ratio of 17.3:1 (determined by inductively coupled plasma-atomic emission spectroscopy (ICP-AES)). Rh(acac)₃ (4.5 mg, 0.011 mmol) and Pt(acac)₂ (27.5 mg, 0.070 mmol) were used for the synthesis of Rh-doped Pt NWs with a Pt/Rh atomic ratio of 6.2:1 (determined by ICP-AES).

Electrochemical Measurements. Before preparation of carbon-supported catalysts, the as-prepared Pt-based NWs were collected by centrifugation and washed four times with hexane. The NWs were then loaded on a carbon support (Vulcan XC-72) with a Pt loading content of 20% (determined by ICP-AES). Typically, 4.0–4.4 mg of NWs (keeping 4.0 mg of Pt in all samples determined by ICP-AES) dispersed in 5 mL of hexane and 16.0 mg of Vulcan XC-72 carbon dispersed in 20 mL of hexane were mixed and stirred overnight. The loaded catalysts were then collected by centrifugation, redispersed in 10 mL of acetic acid, and heated at 70 °C for 2 h to clean the surface of the NWs. Afterward, the catalysts were recovered by centrifugation, followed by washing with ethanol three times. After being dried, 1.0 mg of the catalyst was redispersed in a mixture containing 0.745 mL of deionized water, 0.250 mL of isopropyl alcohol, and 0.005 mL of Nafion (5%) to form homogeneous catalyst ink by sonicating for 2 h. Then, 10 μL of the suspension was deposited on a glassy carbon rotating disk electrode (RDE) with a geometric area of 0.196 cm². For the commercial Pt/C catalysts (20 wt % loading, Johnson Matthey), the dispersion solution (5 mg/mL) was prepared and sonicated for 1

h. Next, 3.5 μL of the dispersion was then deposited onto a glassy carbon RDE with a geometric area of 0.196 cm².

Electrochemical measurements were carried out with a three-electrode system on an IM6 electrochemical workstation (Zahner, Germany). A Pt wire and Ag/AgCl electrode were used as the counter and reference electrodes, respectively. All potentials were converted to values with reference to reversible hydrogen electrode (RHE). The CV measurements were processed in HClO₄ (0.1 M) solutions under a flow of N₂ at a sweep rate of 50 mV s⁻¹. The ORR measurements were performed in O₂-saturated 0.1 M HClO₄ at a rotation rate of 1600 rpm and a sweep rate of 10 mV s⁻¹. Durability test was performed at room temperature by applying cyclic sweeps between 0.6 and 1.1 V_{RHE} in 0.1 M HClO₄ at a sweep rate of 100 mV s⁻¹. The mass and specific activities were obtained by normalizing the kinetic current densities to the loading Pt mass and real active surface area.

For the CO stripping voltammogram, the electrode with deposited catalyst was first kept in CO-saturated 0.5 M H₂SO₄ electrolyte at the potential of 0.1 V_{RHE} for 20 min to adsorb monolayer CO molecules. Afterward, the electrode was transferred to another cell filled with fresh 0.5 M H₂SO₄ electrolyte (without CO). The CO stripping was recorded in the potential range of 0.05 to 1.2 V_{RHE} at a scan rate of 50 mV s⁻¹.

CO Pulse Chemisorption. The CO pulse chemisorption experiments were performed using a Micromeritics Chemisorption Analyzer (AutoChem II) under a flow of 10 mL min⁻¹ helium as carrier gas. For each catalyst, an amount of 5–10 mg was mounted between quartz wool in a sample tube assembling in a furnace. The temperature was measured by a thermocouple at the sample position. Before the pulse measurement, each catalyst should be pretreated in 10% (v/v) H₂–Ar flow (20 mL min⁻¹) at 350 °C for 30 min to remove any surface contamination and then cooled to 20 °C by purging pure He (10 mL min⁻¹). In the step of pulse chemisorption, 0.525 mL of 10% (v/v) CO–He flow was pulsed over the catalyst bed every 5 min at 20 °C. The dispersion of Pt atoms was evaluated from the thermal conductivity detector (TCD) signals by assuming a Pt/CO stoichiometry of 1.

XAFS. The XAFS spectra at Pt L₃-edge ($E_0 = 11\,564$ eV) were performed at BL14W1 beamline of Shanghai Synchrotron Radiation Facility (SSRF) operated at 3.5 GeV under “top-up” mode with a constant current of 220 mA. The XAFS data on Pt samples were recorded under transmission mode with ion chambers. The energy was calibrated accordingly to the absorption edge of pure Pt foil. Athena and Artemis codes were used to extract the data and fit the profiles. For the EXAFS part, the Fourier transformed (FT) data in *R* space were analyzed by applying the metallic Pt model for the Pt–Pt. The passive electron factor, S_0^2 , was determined by fitting the experimental Pt foil data and fixing the Pt–Pt coordination number at 12 and then fixed for further analysis of the measured samples. The parameters describing the electronic properties, e.g., correction to the photoelectron energy origin, E_0 , and local structure environment including coordination number (CN), bond distance (*R*), and Debye–Waller factor around the absorbing atoms were allowed to vary during the fit process. The fitted ranges for *k* and *R* spaces were selected to be $k = 3\text{--}13$ Å⁻¹ and $R = 1.3\text{--}3.1$ Å (*k*²-weighted), respectively.

DFT Calculations. All calculations were performed using the VASP code.³⁹ The electron–ion interactions were described by projector augmented wave potentials.⁴⁰ The exchange–correlation function was described by the generalized gradient approximation of Perdew, Burke, and Ernzerhof (GGA-PBE).⁴¹ The electron wave function was expanded using plane waves with an energy cutoff of 400 eV. A vacuum region about 15 Å to the surface was added to ensure decoupling between next slabs. Monkhorst–Pack *k*-meshes (9 × 9 × 1 and 5 × 5 × 1) were adopted for 2 × 2 and 4 × 4 Pt (111) cell, respectively.⁴² Geometric optimization was performed until energy and forces were less than 10⁻⁵ eV and 0.01 eV Å⁻¹. The optimized lattice constant of Pt is 3.97 Å, which is agreement with the experimental value of 3.92 Å. On the basis of the experiment results, two Pt atoms in the 2 × 2 Pt (111) cell with four layers (16 atoms) are replaced by two Rh atoms to form Pt₂Rh in order to reach the estimated atomic ratio of Pt/Rh (6.9:1). The configurations of Rh

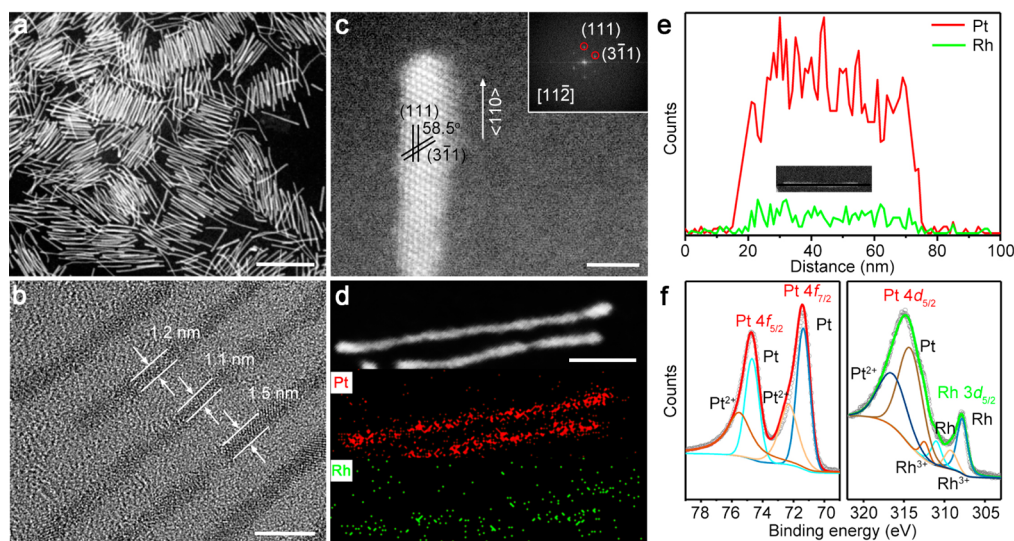


Figure 1. Structural and compositional characterizations of ultrathin Rh-doped Pt NWs. (a) HAADF-STEM image. Scale bar, 50 nm. (b) TEM image. Scale bar, 5 nm. (c) Atomic-resolution HAADF-STEM image. The inset shows the corresponding FFT pattern. Scale bar, 2 nm. (d) EDX mapping of Pt and Rh. Scale bar, 10 nm. (e) EDX line-scanning profile. (f) Pt and Rh XPS spectra recorded from Rh-doped Pt NWs.

atoms in 2×2 Pt (111) are relaxed by considering four different doping positions: (1) One Rh atom is in the first layer and the other one is at the diagonal site in the second layer. (2) One Rh atom is in the first layer, and the other one is adjacent to the first Rh atom in the second layer. (3) Two Rh atoms are in the first layer. (4) Two Rh atoms are in the second layer. After being relaxed, the lowest energy of Pt₇Rh (111) configuration is such that both Rh atoms are in the second layer. In this case, the compressive strain is 0.54% when compared with that of 2×2 Pt (111). Then, we adopted the 2×2 Pt (111) and the most stable Pt₇Rh (111) to study OH adsorption. OH molecules were relaxed by adsorbed on the top site, *hcp* site, *fcc* site, and bridge site, respectively. The energy difference between different sites is very small in the same slab. Because the water stabilizes OH adsorption on the top site,²⁹ only ΔE_{OH} on the top site is considered. The binding energy of OH was performed using the equation $\Delta E_{\text{OH}} = E_{\text{OH}} - (E_{\text{H}_2\text{O}} - 1/2E_{\text{H}_2}) - E$,²⁹ where E and E_{OH} are the energies of (111) slab and (111) surface with OH adsorbed, respectively. For the vacancy formation energy ($\Delta E_{\text{vac}} = E_{\text{vac}} - E + \mu_{\text{Pt}}$) of Pt atoms,⁴³ we compared ΔE_{vac} of Pt (111) and Pt₇Rh (111) slabs to reveal the effects of Rh doping. E_{vac} is the energy of slabs with one Pt vacancy on the surface, and E is the energy of perfect slab (there are two different vacancy positions in the Pt₇Rh (111) slab). We also calculated the projected *d*-density of states and *d*-band centers for 2×2 Pt (111) and Pt₇Rh (111) slabs. All of the above slabs were with four atomic layers fully relaxed, and during studies of OH adsorption, vacancy formation energy, and projected *d*-density of states, the shape and size of the cell were fixed.

Characterization Techniques. Transmission electron microscopy (TEM), high-angle annular dark-field scanning transmission electron microscopy (HAADF-STEM) images, and energy-dispersive X-ray spectroscopy (EDX) analyses were collected on a JEOL ARM-200F field-emission transmission electron microscope operating at 200 kV accelerating voltage. X-ray diffraction (XRD) characterization was performed using a Philips X'Pert Pro X-ray diffractometer with a monochromatized Cu K α radiation source and a wavelength of 0.1542 nm. XPS analysis was carried out on an ESCALAB 250 X-ray photoelectron spectrometer with Al K α as the excitation source. The metal concentrations of Pt and Rh were determined by ICP-AES (Atomscan Advantage, Thermo Jarrell Ash, USA). Fourier transform infrared (FT-IR) spectra were recorded from 3000 to 600 cm^{-1} on a Nicolet 380 FTIR spectrometer (Thermo Electron).

RESULTS AND DISCUSSION

Synthesis and Structural Characterizations. In a typical synthesis, the oleylamine solution containing a certain amount of Pt(acac)₂, Rh(acac)₃, and dodecyltrimethylammonium bromide (DDAB) in a 20 mL vial was preheated in an oil bath at 180 °C for 5 min. W(CO)₆ was subsequently added into the preheated solution to initiate the reaction. The products were obtained after the reaction had proceeded for another 2 h. Figure 1a,b, respectively, shows the representative HAADF-STEM and TEM images of the as-obtained products, demonstrating the formation of ultrathin 1D NWs in high purity and uniformity. The average diameter and length of the NWs were determined as 1.3 ± 0.3 nm and 40.4 ± 15.1 nm, respectively (Figure S1). The atomic-resolution HAADF-STEM image (Figure 1c) recorded from an individual NW shows that the diameter of NW was about seven atomic layers, consistent with the average diameter. The well-defined fringes corresponding with {111} and {311} planes of face-centered cubic (*fcc*) Pt and the growth direction of <110> were distinguished, matching the fast Fourier transform (FFT) pattern shown in the inset. Both the elemental mapping (Figure 1d) and line-scanning profile (Figure 1e) obtained using EDX indicate a homogeneous distribution of Rh and Pt throughout the NW. X-ray photoelectron spectroscopy (XPS) analysis (Figures 1f and S2) confirms the presence of Pt and Rh in the obtained NWs. As shown in Figure 1f, the peaks at 74.7 and 71.4 eV were assigned to the metallic Pt 4f_{5/2} and Pt 4f_{7/2} peaks. Furthermore, the atomic ratio of Pt/Rh was estimated to be 6.8:1 by XPS, in line with the value of 6.9:1 determined by ICP-AES. The XRD peaks (Figure S3) of the NWs show slight blue-shifts with regards to *fcc* Pt, in accordance with the small fraction of incorporated Rh atoms in NWs.

For comparison, we also synthesized the Pt NWs by using the standard procedure without introducing Rh precursor. The morphological and structural analysis (Figure S4a–e) proves the production of Pt NWs with an average diameter of 1.8 ± 0.3 nm and length of 38.3 ± 14.3 nm. The atomically resolved HAADF-STEM image verifies the growth direction of <110> for such Pt NWs, which is identical to that of Rh-doped Pt NWs. The Pt 4f XPS spectrum (Figure S4f) recorded from Pt

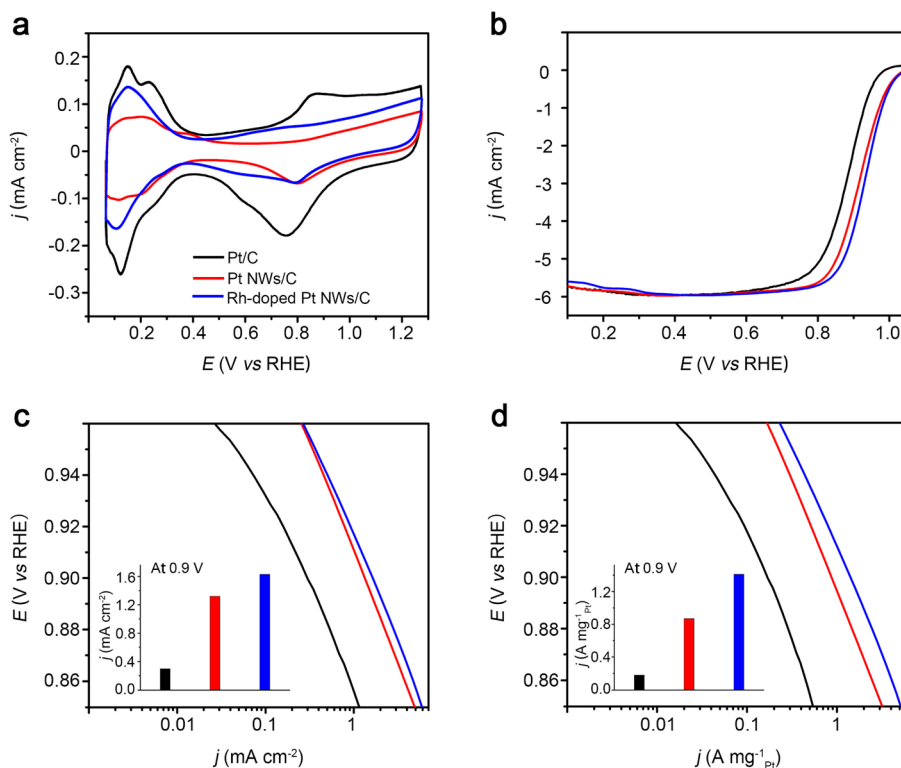


Figure 2. Comparison of electrocatalytic activity between the Rh-doped Pt NWs/C, Pt NWs/C, and commercial Pt/C. (a) Cyclic voltammograms recorded at room temperature in a N_2 -purged 0.1 M HClO_4 solution with a sweep rate of 50 mV s^{-1} . (b) Corresponding positive-going ORR polarization curves recorded in an O_2 -saturated 0.1 M HClO_4 solution with a sweep rate of 10 mV s^{-1} and a rotation rate of 1600 rpm. (c, d) Specific and mass ORR activities given as kinetic current densities normalized to the ECSAs and Pt masses of the catalysts, respectively. The color scheme in (a) applies to all other panels.

NWs illustrates that the surface Pt is mainly in metallic state and shows the Pt $4f_{7/2}$ peak position at 71.2 eV. Compared to the Pt $4f_{7/2}$ peak position of Pt NWs, the Pt $4f_{7/2}$ binding energy of Rh-doped Pt NWs is obviously blue-shifted, indicating the negative charge transfer from Pt to Rh. In addition, Rh-doped Pt NWs with different Pt/Rh atomic ratios of 17.3:1 and 6.2:1 were synthesized by adding different amounts of $\text{Pt}(\text{acac})_2$ and $\text{Rh}(\text{acac})_3$ (Figures S5 and S6). As it is challenging to analyze the exposed facets on the surfaces of NWs by electron microscopy techniques, we thus employed CO stripping voltammetry, a surface-sensitive tool, to determine the surface facets.^{44–46} The CO stripping potential on the Pt NWs is at 0.87 V versus reversible hydrogen electrode (V_{RHE}) (Figure S7), which indicates the surface of Pt NWs is dominated by {111} facets.⁴⁴ Because of the interference from incorporated Rh atoms, we cannot directly determine the surface facets of Rh-doped Pt NWs by using CO stripping. However, it is rational to assume that the Rh-doped Pt NWs expose similar surface facets with Pt NWs due to their identical growth direction and similar morphology.

As such a thin diameter generally leads to a high UE of Pt atoms, we further calculated the UE of Pt atoms for the as-synthesized Rh-doped Pt NWs, Pt NWs, and commercial Pt/C nanoparticles (an average size of $\sim 3 \text{ nm}$). To facilitate the estimation of UEs, approximate geometrical models of the Rh-doped Pt NWs, Pt NWs, and Pt/C nanoparticles (Figure S8a–e) were established on the basis of the structural information acquired from Figure 1. Because the UE of Pt atoms in a specific NW is identical to that in a subunit extracted along the $\langle 110 \rangle$ direction of NW, the UE of Pt atoms can be worked out

by counting the UE in an equivalent subunit. Owing to the small fraction of Rh atoms and the random atomic arrangement, the influence of Rh atoms on the UE of Pt atoms for the Rh-doped Pt NWs could be neglected. As a result, the UE of Pt atoms for the Rh-doped Pt NWs was estimated to be of 48.6%. It should be noted that such a value of UE is comparable to that of nanosheets with thickness of four atomic layers (50%), displaying an advantageous structural feature. For comparison, the UEs of Pt atoms for Pt NWs and commercial Pt/C nanoparticles were determined to be of 35.0 and 30.6%, respectively.

Formation Mechanism. The mechanism responsible for the formation of Rh-doped Pt NWs was also elucidated in detail. Samples obtained at different stages during the standard synthesis procedure were examined by TEM and ICP-AES to figure out the morphological and compositional evolution for Rh-doped Pt NWs (Figures S9 and S10). At an early reaction stage of 30 s, abundant small nanocrystals were observed. These nanocrystals are mainly composed of Pt based on the ICP-AES result, implying the preferential reduction of Pt precursor. As the reaction time was extended to 2 min, essentially all the small particles evolved into short nanorods with an average length of 13.1 nm, as well as the increased atomic percents of Rh. Upon continually increasing the reaction time to 2 h, these nanorods further grew into NWs with a higher aspect ratio. The length of NWs was found to remain almost unchanged when the reaction time exceeded 2 h, consistent with their invariable composition. The time-dependent observations clearly indicate the anisotropic growth of nanocrystals to form the NWs.

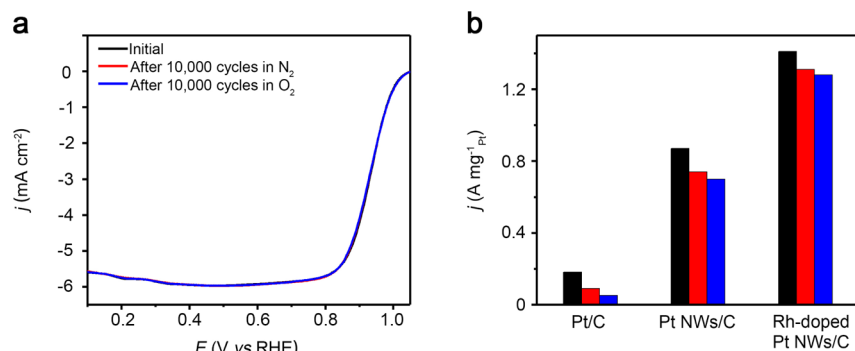


Figure 3. Durability of Rh-doped Pt NWs/C. (a) Corresponding ORR polarization curves for the carbon-supported Rh-doped Pt NWs before and after ADTs of 10 000 cycles in N₂ and O₂ conditions. (b) Comparison of durability between the carbon-supported Rh-doped Pt NWs, carbon-supported Pt NWs, and the commercial Pt/C. The comparison is based on the mass activities at 0.9 V_{RHE}. The color scheme in (a) applies to both panels.

Generally, the anisotropic growth for *fcc* metal nanocrystals can be attributed to the defect-induced growth and/or template-directed growth.⁴⁷ In our case, the perfect single-crystal structure revealed by atomically resolved HAADF-STEM has ruled out the former mechanism. Moreover, the FT-IR spectrum of the Rh-doped Pt NWs (Figure S11) corresponds well to the signal of DDAB, suggesting that DDAB is adsorbed at the surface of the NWs. Since DDAB can function as a soft template on the basis of the previous reports,⁴⁸ we thus studied the effects of surfactant on the morphology of products to verify the template-directed formation mechanism for the Rh-doped Pt NWs. Dodecyltrimethylammonium bromide (DTAB), which is very similar to DDAB except for the different carbon number of the alkyl chain (Scheme S1), was used to replace DDAB while maintaining other parameters as unchanged. The TEM image of as-prepared products (Figure S12a) proves the formation of NWs with an average diameter of 1.8 nm and length of 39.9 nm. However, when KBr was substituted for DDAB, irregular particles were generated (Figure S12b), suggesting the critical role of surfactant.

The amount of W(CO)₆ was also found to influence the morphology of products, as shown in Figure S13. Because W(CO)₆ was the reductant for the synthesis, the results indicate that the faster reduction kinetics favors the formation of such NWs, in line with previous reports on the synthesis of NWs based on template-directed growth mode.⁴⁹ As regards the explicit function of reduction kinetics, we assume that the reduction kinetics may affect the formation of reverse-micelle-like structure by controlling the concentration of free DDAB molecules in the reaction solution. Specifically, the Pt precursor can complex a large amount of DDAB molecules before reducing to Pt atoms. The faster reduction kinetics leads to the release of more free DDAB molecules to the reaction solution and thus facilitates the formation of reverse-micelle-like structure, which directs the growth of NWs. Combining these experimental results, it is convincing to ascribe the formation of Rh-doped Pt NWs to a template-directed growth mechanism, where the surfactant-like DDAB acts as a soft template. The schematic diagram (Figure S14) explicitly illustrates the surfactant-directed growth process for Rh-doped Pt NWs. Briefly, the DDAB molecules tend to self-organize into an elongated reverse-micelle-like structure, in which the Rh-doped Pt particle is formed. Because of the lower packing density of DDAB molecules at the ends of Pt particle, the reduced Pt and

Rh atoms could be successively deposited along this direction to generate an anisotropic NW.

ORR Performance. The electrocatalytic ORR performances of Pt-based NWs were evaluated using the rotating disk electrode (RDE) method. Prior to deposition on RDE, the catalyst was prepared by loading the sample on Vulcan XC-72 carbon support and then was treated with acetic acid to clean the surface. For comparison, the ORR properties of commercial Pt/C (JM) (20 wt % Pt nanoparticles with an average size of ~3 nm on Vulcan XC-72 carbon) were also measured. Figure 2a shows the cyclic voltammograms (CVs) of different catalysts conducting at room temperature in a N₂-saturated 0.1 M HClO₄ solution at a sweep rate of 50 mV s⁻¹ in the potential range of 0.06–1.26 V_{RHE}. On the basis of the charge associated with the desorption of hydrogen, we can obtain the ECSA of each catalyst. The specific ECSA was then obtained by normalizing ECSA against Pt mass. Because of the thinnest diameter of Rh-doped Pt NWs, the specific ECSA of Rh-doped Pt NWs/C catalyst (86.4 m² g⁻¹_{Pt}) was much higher than those of Pt NWs/C catalyst (65.3 m² g⁻¹_{Pt}) and commercial Pt/C (60.9 m² g⁻¹_{Pt}). The trend of measured ECSA for these catalysts is consistent with the trend of catalytic sites estimated by CO pulse chemisorption experiments and model calculations (Figure S15). To compare the catalytic activities of these catalysts toward ORR, the positive-going ORR polarization curves were recorded at room temperature in an O₂-saturated 0.1 M HClO₄ solution, as shown in Figure 2b. The specific and mass activities of these catalysts were then extracted by normalizing the kinetic current densities, which were obtained according to the Koutecky–Levich equation, against the ECSA and Pt mass, respectively (Figure 2, c and d). Clearly, the Rh-doped Pt NWs/C catalyst exhibited the highest specific and mass activities among these catalysts. At 0.9 V_{RHE}, the specific activity of Rh-doped Pt NWs/C catalyst was 1.63 mA cm⁻², which was 1.2 times higher than that of Pt NWs/C catalyst (1.32 mA cm⁻²) and 5.4 times higher than that of commercial Pt/C (0.30 mA cm⁻²). Due to the higher specific activity and UE of Pt atoms, the mass activity exhibited by Rh-doped Pt NWs/C catalyst (1.41 A mg⁻¹_{Pt}) at 0.9 V_{RHE} was 1.6 times greater than that of Pt NWs/C catalyst (0.87 A mg⁻¹_{Pt}) and 7.8 times greater than that of commercial Pt/C (0.18 A mg⁻¹_{Pt}). To explore the optimum composition of Rh-doped Pt NWs toward ORR, we also measured the ORR activities of Rh-doped Pt NWs/C catalysts with different Pt/Rh atomic ratios, as shown in Figure S16. Clearly, the Rh-doped Pt NWs/C catalyst

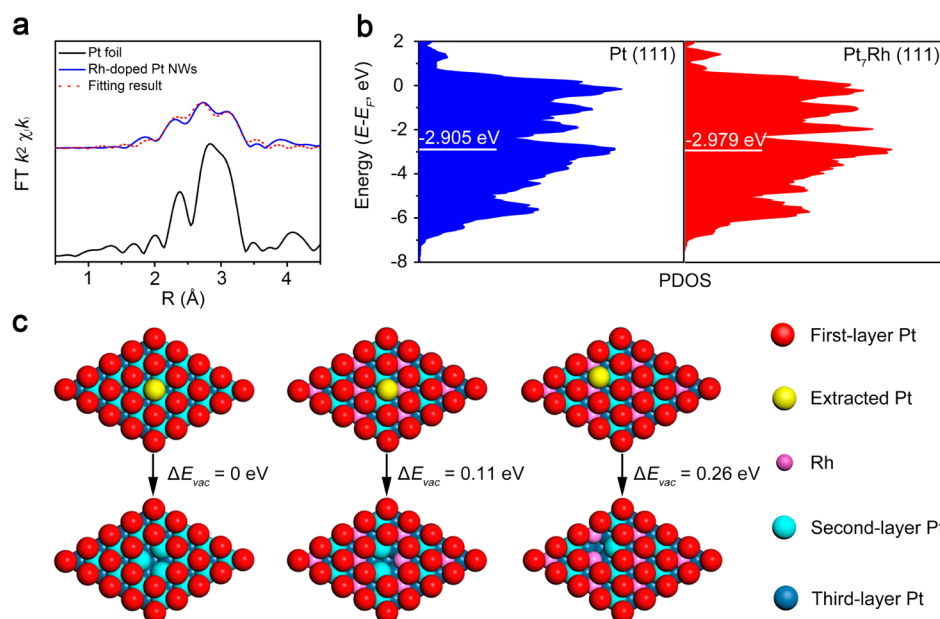


Figure 4. Understanding of the enhanced activity and durability by EXAFS analysis and DFT calculations. (a) Pt L₃-edge EXAFS spectra (blue) in *R* space for Rh-doped Pt NWs with the corresponding fitted curve (red) and Pt foil references (black). (b) Projected *d*-density of states of surface atoms on Pt (111) and Pt₇Rh (111) slabs. The calculated *d*-band centers are marked with white lines. (c) DFT result shows the different formation energy of Pt vacancy (ΔE_{vac}). From left to right, the models correspond to ΔE_{vac} of Pt (111) slab (left), ΔE_{vac} of Pt₇Rh (111) slab calculated by extracting a Pt atom which bonds with two second-layer Pt atoms (middle), and ΔE_{vac} of Pt₇Rh (111) slab calculated by extracting a Pt atom which bonds with two second-layer Rh atoms (right), respectively. Note that ΔE_{vac} of Pt (111) slab was defined as a zero point.

with a Pt/Rh atomic ratio of 6.9:1 presents the highest activity. The results also indicate a volcano-like relationship between the ORR activity and the amount of doped Rh atoms, which can be generally interpreted by using the Sabatier principle.⁵⁰

Another important indicator of a catalyst for practical application is its long-term durability. Thus, the durability of different catalysts was evaluated through an accelerated durability test (ADT) at room temperature. As shown in Figure 3a, negligible shifts of the positive-going ORR polarization curves were observed for the Rh-doped Pt NWs/C catalyst before and after the tests. After 10 000 cycles in O₂ condition, the Rh-doped Pt NWs/C catalyst still retained a mass activity up to 1.28 A mg⁻¹_{Pt} with a drop of 9.2% (Figure 3b). By contrast, the Pt NWs/C and commercial Pt/C catalysts lost 19.5 and 72.3% of their initial mass activities (Figures 3b and S17), respectively. Notably, even compared with most of the recently reported Pt-based electrocatalysts (Table S1), the Rh-doped Pt NWs/C catalyst showed a great advantage in the long term durability. The morphologies of these catalysts before and after 10 000 electrochemical cycles were also examined by TEM (Figure S18). Strikingly, the commercial Pt/C catalyst showed severe sintering during the durability test. With respect to the serious aggregation for commercial Pt/C catalyst, the morphology of Rh-doped Pt NWs/C catalyst showed a negligible change after 10 000 cycles, indicating superior stability of the structure.

Understanding of the Enhanced Activity and Stability. In order to understand the enhanced specific activity of Rh-doped Pt NWs/C catalyst, we explored the local structure of Pt atoms by measuring the EXAFS (Figure 4a and Table S2). The results reveal that the Pt–Pt bond length in Rh-doped Pt NWs (2.74 Å) is ~0.7% shorter than that of Pt foil (2.76 Å), which is reasonable considering the ultrathin diameter of NWs and smaller radius of Rh atoms. Such compressive strain may improve the specific activity by weakening the adsorption

energy of hydroxyl (ΔE_{OH}) up to ~0.02 eV according to the established relationship between the adsorption energy and lattice strain for Pt.²⁹ The DFT calculations were also performed to rationalize the higher specific activity of Rh-doped Pt NWs. Considering the predominant {111} planes on the surface of NWs and the composition of Rh-doped Pt NWs, we constructed periodic Pt₇Rh (111) slab as a model of Rh-doped Pt NWs. After the convergence test, the Pt₇Rh slab presents 0.54% compressive strain relative to that of Pt (111) slab. Notably, this contraction just contains the effects of the incorporated Rh atoms. The *d*-band center of the Pt₇Rh (111) surface was then calculated and compared with that of Pt (111) surface to understand the difference in ORR activity based on the previously established *d*-band theory.⁵¹ As shown in Figure 4b, the downshifted *d*-band center of Pt₇Rh (111) slab is consistent with the improved specific activity of Rh-doped Pt NWs. In addition, ΔE_{OH} of Pt (111) and Pt₇Rh (111) slabs were also compared considering that an ΔE_{OH} of ~0.1 eV weaker than Pt (111) can yield the optimum ORR activity based on the previous studies.⁵² Our DFT calculations reveal that the Pt₇Rh (111) slab shows an ΔE_{OH} that is 0.03 eV weaker than that of the Pt (111) slab, supporting the experimental observations again. As indicated by the EXAFS analysis and DFT calculations, the integration of strain effect and ligand effect contributed the observed higher specific activity of Rh-doped Pt NWs.

On the basis of our experimental results, the best durability of Rh-doped Pt NWs/C catalyst can be ascribed to the combination of unique 1D anisotropic structure and a small amount of incorporated Rh atoms. Specifically, the unique 1D anisotropic structure generally shows an intrinsically excellent structural stability by retarding the dissolution and ripening processes.³¹ Furthermore, the higher surface area of ultrathin NWs strengthens the contact between ultrathin NWs and the carbon support,³⁶ benefiting the structural stability of catalyst.

More importantly, the small amount of incorporated Rh atoms can suppress the dissolution of Pt atoms by preferentially sacrificing Rh atoms during the operation condition.³⁷ The ICP-AES result revealed that the Pt/Rh ratio after 10 000 cycles was reduced to 7.7:1, confirming that Rh, rather than Pt, was leached out during the electrochemical treatment owing to a lower redox potential (1.188 V_{RHE} for Pt²⁺/Pt and 0.8 V_{RHE} for Rh³⁺/Rh).^{53,54}

We further performed DFT calculations to shed light on the enhanced durability of Rh-doped Pt NWs. Since the instability of Pt-based ORR catalysts under the operating condition is mainly due to the oxidation and dissolution of Pt atoms into Pt²⁺ ions, the vacancy formation energy (ΔE_{vac}) of Pt atoms can be regarded as a descriptor to reflect the durability of Pt-based catalysts.⁵⁵ We thus compared ΔE_{vac} of Pt (111) and Pt₇Rh (111) slabs to provide the insight into the effect of incorporated Rh atoms on durability. As shown in Figure 4c, the Pt₇Rh (111) slab shows ΔE_{vac} that is obviously higher than that of the Pt (111) slab, no matter which type of Pt atom is extracted, confirming the better durability after the incorporation of Rh atoms. In other words, the incorporated Rh atoms enhanced the durability of Pt-based catalysts by improving the oxidation-resistant ability of Pt atoms.

CONCLUSIONS

We have demonstrated a remarkable ORR catalyst with both excellent mass activity and durability based on ultrathin Rh-doped Pt NWs by combining the merits of high UE of Pt atoms, anisotropic 1D NW, and doping of Rh atoms. The surfactant-directed growth mechanism was concluded to be responsible for the formation of such ultrathin NWs. Because of the ultrathin diameter of 1.3 nm, the UE of Pt atoms for the NWs was estimated to be as high as 48.6%. Compared with commercial Pt/C catalyst, the Rh-doped Pt NWs/C catalyst shows a 7.8- and 5.4-fold enhancement in mass activity and specific activity, respectively. The combination of EXAFS analysis and DFT calculations reveals that compressive strain and ligand effect in Rh-doped Pt NWs optimize the adsorption energy of hydroxyl and in turn enhance the specific activity. Moreover, even after 10 000 cycles of accelerated durability test in O₂ condition, the Rh-doped Pt NWs/C catalyst exhibits a drop of 9.2% in mass activity, compared to a big decrease of 72.3% for commercial Pt/C. The improved durability can be rationalized by the increased vacancy formation energy of Pt atoms in Rh-doped Pt NWs. We believe that this work not only provides a promising ORR catalyst to advance the practical applications of electrochemical devices but also offers a general strategy to design optimized heterogeneous catalysts.

ASSOCIATED CONTENT

Supporting Information

The Supporting Information is available free of charge on the ACS Publications website at DOI: 10.1021/jacs.7b01036.

Diameter and length distributions, XPS spectrum, XRD patterns, structural characterization of Pt NWs and Rh-doped Pt NWs, CO stripping voltammogram, approximate geometrical models for Rh-doped Pt NWs, TEM images, time-dependent compositional evolution data, FT-IR spectra, mechanism and formula schematics, chemisorption profiles, cyclic voltammograms, ORR polarization curves, performance of Rh-doped Pt NWs/C catalyst, and EXAFS data fitting results (PDF)

AUTHOR INFORMATION

Corresponding Authors

*E-mail: sirui@sinap.ac.cn.

*E-mail: zpeng@uakron.edu.

*E-mail: zengj@ustc.edu.cn.

ORCID

Zhenmeng Peng: 0000-0003-1230-6800

Jie Zeng: 0000-0002-8812-0298

Author Contributions

H.H. and K.L. contributed equally to this work.

Notes

The authors declare no competing financial interest.

ACKNOWLEDGMENTS

This work was supported by Collaborative Innovation Center of Suzhou Nano Science and Technology, MOST of China (2014CB932700), NSFC (21603208, 21573206, 21373259, and 51371164), China Postdoctoral Science Foundation (2015M580536 and 2016T90569), Strategic Priority Research Program of the CAS (XDB01020000 and XDA09030102), Key Research Program of Frontier Sciences of the CAS (QYZDB-SSW-SLH017), the Hundred Talents project of the CAS, and Fundamental Research Funds for the Central Universities.

REFERENCES

- (1) Debe, M. K. *Nature* **2012**, *486*, 43–51.
- (2) Steele, B. C. H.; Heinzel, A. *Nature* **2001**, *414*, 345–352.
- (3) Wang, Y. J.; Wilkinson, D. P.; Zhang, J. J. *Chem. Rev.* **2011**, *111*, 7625–7651.
- (4) Holewinski, A.; Idrobo, J. C.; Linic, S. *Nat. Chem.* **2014**, *6*, 828–834.
- (5) Wu, J. B.; Yang, H. *Acc. Chem. Res.* **2013**, *46*, 1848–1857.
- (6) Zhang, H.; Jin, M.; Xia, Y. *Chem. Soc. Rev.* **2012**, *41*, 8035–8049.
- (7) Rabis, A.; Rodriguez, P.; Schmidt, T. J. *ACS Catal.* **2012**, *2*, 864–890.
- (8) Choi, D. S.; Robertson, A. W.; Warner, J. H.; Kim, S. O.; Kim, H. *Adv. Mater.* **2016**, *28*, 7115–7122.
- (9) Lee, D. H.; Lee, W. J.; Lee, W. J.; Kim, S. O.; Kim, Y. *Phys. Rev. Lett.* **2011**, *106*, 175502.
- (10) Lee, W. J.; Choi, D. S.; Lee, S. H.; Lim, J.; Kim, J. E.; Li, D. J.; Lee, G. Y.; Kim, S. O. *Part. Part. Syst. Charact.* **2014**, *31*, 965–970.
- (11) Perez-Alonso, F. J.; McCarthy, D. N.; Nierhoff, A.; Hernandez-Fernandez, P.; Strebler, C.; Stephens, I. E. L.; Nielsen, J. H.; Chorkendorff, I. *Angew. Chem., Int. Ed.* **2012**, *51*, 4641–4643.
- (12) Shao, M.; Peles, A.; Shoemaker, K. *Nano Lett.* **2011**, *11*, 3714–3719.
- (13) Zhao, X.; Chen, S.; Fang, Z.; Ding, J.; Sang, W.; Wang, Y.; Zhao, J.; Peng, Z.; Zeng, J. *J. Am. Chem. Soc.* **2015**, *137*, 2804–2807.
- (14) Koeningmann, C.; Zhou, W.; Adzic, R. R.; Sutter, E.; Wong, S. S. *Nano Lett.* **2010**, *10*, 2806–2811.
- (15) Ruan, L.; Zhu, E.; Chen, Y.; Lin, Z.; Huang, X.; Duan, X.; Huang, Y. *Angew. Chem., Int. Ed.* **2013**, *52*, 12577–12581.
- (16) Zhang, J.; Vukmirovic, M. B.; Xu, Y.; Mavrikakis, M.; Adzic, R. R. *Angew. Chem., Int. Ed.* **2005**, *44*, 2132–2135.
- (17) Xie, S.; Choi, S. I.; Lu, N.; Roling, L. T.; Herron, J. A.; Zhang, L.; Park, J.; Wang, J.; Kim, M. J.; Xie, Z.; Mavrikakis, M.; Xia, Y. *Nano Lett.* **2014**, *14*, 3570–3576.
- (18) Sasaki, K.; Naohara, H.; Choi, Y.; Cai, Y.; Chen, W. F.; Liu, P.; Adzic, R. R. *Nat. Commun.* **2012**, *3*, 1115.
- (19) Chen, C.; Kang, Y.; Huo, Z.; Zhu, Z.; Huang, W.; Xin, H. L.; Snyder, J. D.; Li, D.; Herron, J. A.; Mavrikakis, M.; Chi, M.; More, K. L.; Li, Y.; Markovic, N. M.; Somorjai, G. A.; Yang, P.; Stamenkovic, V. R. *Science* **2014**, *343*, 1339–1343.

- (20) Zhang, L.; Roling, L. T.; Wang, X.; Vara, M.; Chi, M.; Liu, J.; Choi, S. I.; Park, J.; Herron, J. A.; Xie, Z.; Mavrikakis, M.; Xia, Y. *Science* **2015**, *349*, 412–416.
- (21) Chen, S.; Su, H.; Wang, Y.; Wu, W.; Zeng, J. *Angew. Chem., Int. Ed.* **2015**, *54*, 108–113.
- (22) Fang, Z.; Wang, Y.; Liu, C.; Chen, S.; Sang, W.; Wang, C.; Zeng, J. *Small* **2015**, *11*, 2593–2605.
- (23) Stamenkovic, V. R.; Fowler, B.; Mun, B. S.; Wang, G.; Ross, P. N.; Lucas, C. A.; Markovic, N. M. *Science* **2007**, *315*, 493–497.
- (24) Stamenkovic, V. R.; Mun, B. S.; Arenz, M.; Mayrhofer, K. J. J.; Lucas, C. A.; Wang, G.; Ross, P. N.; Markovic, N. M. *Nat. Mater.* **2007**, *6*, 241–247.
- (25) Huang, X.; Zhao, Z.; Cao, L.; Chen, Y.; Zhu, E.; Lin, Z.; Li, M.; Yan, A.; Zettl, A.; Wang, Y. M.; Duan, X.; Mueller, T.; Huang, Y. *Science* **2015**, *348*, 1230–1234.
- (26) Zhang, C.; Sandorf, W.; Peng, Z. *ACS Catal.* **2015**, *5*, 2296–2300.
- (27) Yu, T.; Kim, D. Y.; Zhang, H.; Xia, Y. *Angew. Chem., Int. Ed.* **2011**, *50*, 2773–2777.
- (28) Wang, H.; Xu, S.; Tsai, C.; Li, Y.; Liu, C.; Zhao, J.; Liu, Y.; Yuan, H.; Abild-Pedersen, F.; Prinz, F. B.; Nørskov, J. K.; Cui, Y. *Science* **2016**, *354*, 1031–1036.
- (29) Escudero-Escribano, M.; Malacrida, P.; Hansen, M. H.; Vej-Hansen, U. G.; Velázquez-Palenzuela, A.; Tripkovic, V.; Schiøtz, J.; Rossmeisl, J.; Stephens, I. E. L.; Chorkendorff, I. *Science* **2016**, *352*, 73–76.
- (30) Wu, J.; Qi, L.; You, H.; Gross, A.; Li, J.; Yang, H. *J. Am. Chem. Soc.* **2012**, *134*, 11880–11883.
- (31) Strasser, P.; Koh, S.; Anniyev, T.; Greeley, J.; More, K.; Yu, C.; Liu, Z.; Kaya, S.; Nordlund, D.; Ogasawara, H.; Toney, M. F.; Nilsson, A. *Nat. Chem.* **2010**, *2*, 454–460.
- (32) Nørskov, J. K.; Bligaard, T.; Rossmeisl, J.; Christensen, C. H. *Nat. Chem.* **2009**, *1*, 37–46.
- (33) Stephens, I. E. L.; Bondarenko, A. S.; Grønby, U.; Rossmeisl, J.; Chorkendorff, I. *Energy Environ. Sci.* **2012**, *5*, 6744–6762.
- (34) Chen, Z.; Waje, M.; Li, W.; Yan, Y. *Angew. Chem., Int. Ed.* **2007**, *46*, 4060–4063.
- (35) Koenigsmann, C.; Wong, S. S. *Energy Environ. Sci.* **2011**, *4*, 1161–1176.
- (36) Bu, L.; Guo, S.; Zhang, X.; Shen, X.; Su, D.; Lu, G.; Zhu, X.; Yao, J.; Guo, J.; Huang, X. *Nat. Commun.* **2016**, *7*, 11850.
- (37) Zhang, J.; Sasaki, K.; Sutter, E.; Adzic, R. R. *Science* **2007**, *315*, 220–222.
- (38) Beermann, V.; Gocyla, M.; Willinger, E.; Rudi, S.; Heggen, M.; Dunin-Borkowski, R. E.; Willinger, M. G.; Strasser, P. *Nano Lett.* **2016**, *16*, 1719–1725.
- (39) Kresse, G.; Furthmüller, J. *Phys. Rev. B: Condens. Matter Mater. Phys.* **1996**, *54*, 11169–11186.
- (40) Blöchl, P. E. *Phys. Rev. B: Condens. Matter Mater. Phys.* **1994**, *50*, 17953–17979.
- (41) Perdew, J. P.; Burke, K.; Ernzerhof, M. *Phys. Rev. Lett.* **1996**, *77*, 3865–3868.
- (42) Monkhorst, H. J.; Pack, J. D. *Phys. Rev. B* **1976**, *13*, 5188–5192.
- (43) Alahmed, Z.; Fu, H. *Phys. Rev. B: Condens. Matter Mater. Phys.* **2007**, *76*, 224101.
- (44) Schmidt, T. J.; Gasteiger, H. A.; Stäb, G. D.; Urban, P. M.; Kolb, D. M.; Behm, R. J. *J. Electrochem. Soc.* **1998**, *145*, 2354–2358.
- (45) van der Vliet, D. F.; Wang, C.; Li, D.; Paulikas, A. P.; Greeley, J.; Rankin, R. B.; Strmcnik, D.; Tripkovic, D.; Markovic, N. M.; Stamenkovic, V. R. *Angew. Chem., Int. Ed.* **2012**, *51*, 3139–3142.
- (46) Chen, G.; Xu, C.; Huang, X.; Ye, J.; Gu, L.; Li, G.; Tang, Z.; Wu, B.; Yang, H.; Zhao, Z.; Zhou, Z.; Fu, G.; Zheng, N. *Nat. Mater.* **2016**, *15*, 564–569.
- (47) Xia, Y.; Xiong, Y.; Lim, B.; Skrabalak, S. E. *Angew. Chem., Int. Ed.* **2009**, *48*, 60–103.
- (48) Gao, J.; Bender, C. M.; Murphy, C. J. *Langmuir* **2003**, *19*, 9065–9070.
- (49) Lu, X.; Yavuz, M. S.; Tuan, H.; Korgel, B. A.; Xia, Y. *J. Am. Chem. Soc.* **2008**, *130*, 8900–8901.
- (50) Bligaard, T.; Nørskov, J. K.; Dahl, S.; Matthiesen, J.; Christensen, C. H.; Sehested, J. *J. Catal.* **2004**, *224*, 206–217.
- (51) Stamenkovic, V.; Mun, B. S.; Mayrhofer, K. J. J.; Ross, P. N.; Markovic, N. M. *J. Am. Chem. Soc.* **2006**, *128*, 8813–8819.
- (52) Greeley, J.; Stephens, E. L.; Bondarenko, A. S.; Johansson, T. P.; Hansen, H. A.; Jaramillo, T. F.; Rossmeisl, J.; Chorkendorff, I.; Nørskov, J. K. *Nat. Chem.* **2009**, *1*, 552–556.
- (53) Bard, A. J.; Faulkner, L. R. *Electrochemical Methods: Fundamentals and Applications*; John Wiley & Sons Inc: New York, 2001.
- (54) Zoski, C. G., Ed. *Handbook of Electrochemistry*; Elsevier: Amsterdam, 2007.
- (55) Chung, D. Y.; Jun, S. W.; Yoon, G.; Kwon, S. G.; Shin, D. Y.; Seo, P.; Yoo, J. M.; Shin, H.; Chung, Y. H.; Kim, H.; Mun, B. S.; Lee, K. S.; Lee, N. S.; Yoo, S. J.; Lim, D. H.; Kang, K.; Sung, Y. E.; Hyeon, T. *J. Am. Chem. Soc.* **2015**, *137*, 15478–15485.